

1        **Improved Electrochemical Performance of NaVOPO<sub>4</sub>**  
2        **Positive Electrodes at Elevated Temperature in an Ionic**  
3        **Liquid Electrolyte**

4  
5  
6        Chih-Yao Chen<sup>a</sup>, Kazuhiko Matsumoto<sup>a, \*</sup>, Toshiyuki Nohira<sup>b, \*</sup>, and Rika Hagiwara<sup>a, \*</sup>

7        *<sup>a</sup>Graduate School of Energy Science, Kyoto University, Sakyo-ku, Kyoto 606-8501, Japan*

8        *<sup>b</sup>Institute of Advanced Energy, Kyoto University, Gokasho, Uji, Kyoto 611-0011, Japan*

9  
10  
11  
12        \*Corresponding authors: Kazuhiko Matsumoto, Toshiyuki Nohira, Rika Hagiwara

13        E-mail addresses: [k-matsumoto@energy.kyoto-u.ac.jp](mailto:k-matsumoto@energy.kyoto-u.ac.jp);

14        [nohira.toshiyuki.8r@kyoto-u.ac.jp](mailto:nohira.toshiyuki.8r@kyoto-u.ac.jp); [hagiwara@energy.kyoto-u.ac.jp](mailto:hagiwara@energy.kyoto-u.ac.jp)

15        Tel: +81-75-753-5822

16        Fax: +81-75-753-5906

17

18

19

## 20    **Abstract**

21            Sodium secondary batteries operating in a wide temperature range are  
22            attractive as large-scale energy storage devices, and ionic liquid electrolytes are  
23            suitable for this purpose. In this study, NaVOPO<sub>4</sub> has been investigated as positive  
24            electrode material for Na secondary batteries, and its electrochemical performance  
25            has been examined in the Na[FSA]–[C<sub>3</sub>C<sub>1</sub>pyrr][FSA] ionic liquid (C<sub>3</sub>C<sub>1</sub>pyrr =  
26            *N*-methyl-*N*-propylpyrrolidinium and FSA = bis(fluorosulfonyl)amide) at 298 and  
27            363 K. The NaVOPO<sub>4</sub> electrode exhibits a reversible capacity of 60 and 101 mAh  
28            g<sup>–1</sup> at 298 and 363 K, respectively. Acceptably good rate capability is achieved at  
29            363 K, as 76% of the maximum capacity is maintained at 5 C rate. Cyclability  
30            tests prove good reversibility of the material, in which 74% of the initial specific  
31            capacity maintains over 300 cycles at 363 K. XRD measurements reveal that the  
32            charge–discharge process of NaVOPO<sub>4</sub> involves a single-phase reaction.  
33            Galvanostatic intermittent titration technique (GITT) analysis highlights a  
34            3–5-fold increase of the apparent Na chemical diffusion coefficient in NaVOPO<sub>4</sub>  
35            upon increasing the temperature from 298 to 363 K, which is reflected in the  
36            superior electrochemical performance at 363 K than at 298 K.

37

## 38 1. Introduction

39 Sodium secondary batteries have attracted considerable attention as alternatives  
40 or complements to the prevailing Li-ion batteries, owing to their virtually unlimited  
41 supply, low material cost, and large worldwide availability.<sup>1-3</sup> Research on Na  
42 secondary batteries has continued to gain momentum from the systematic  
43 extrapolation of the well-established knowledge regarding lithium ion batteries. The  
44 larger ionic radii of Na<sup>+</sup> (1.02 Å) than Li<sup>+</sup> (0.76 Å)<sup>3</sup> was formerly deemed to frustrate  
45 the reversible insertion and fast transport of sodium within rigid inorganic hosts.<sup>4</sup>  
46 However, a recent computational study suggested that the diffusion of Na can be  
47 faster than that of Li in certain crystal structures.<sup>5</sup> The milder Lewis acidity of Na<sup>+</sup>  
48 than Li<sup>+</sup> has also been shown to lead to a commonly smaller desolvation energy in  
49 polar solvents.<sup>6-8</sup> Since the desolvation process of alkali ions highly influences their  
50 kinetics of insertion at the electrolyte interface,<sup>9</sup> the relatively low desolvation energy  
51 coupled with the facile bulk diffusion may open up new appealing possibilities for  
52 high-power Na secondary batteries.<sup>3</sup>

53 One of the main issues for Na secondary battery systems is their inferior energy  
54 densities compared to the Li-based ones,<sup>3,5,10</sup> which is caused by (1) the larger mass  
55 (22.99 g mol<sup>-1</sup> for Na and 6.94 g mol<sup>-1</sup> for Li) and (2) the higher redox potential  
56 (-2.71 V vs. SHE for Na<sup>+</sup>/Na and -3.04 V vs. SHE for Li<sup>+</sup>/Li).<sup>10</sup> In order to

counteract these intrinsic limitations, positive electrode materials that enable the realization of high capacity and high operating voltages are essential for Na secondary batteries. In this respect, vanadium-based phosphates are gaining increasing prominence.<sup>10–18</sup> Relatively high operating potentials (vs. Na<sup>+</sup>/Na) were achieved for Na<sub>3</sub>V<sub>2</sub>(PO<sub>4</sub>)<sub>3</sub> (3.4 V),<sup>12,13</sup> Na<sub>3</sub>V<sub>2</sub>(PO<sub>4</sub>)<sub>2</sub>F<sub>3</sub> (3.9 V),<sup>10,11</sup> Na<sub>1.5</sub>VPO<sub>4.8</sub>F<sub>0.7</sub> (3.8 V),<sup>15</sup> Na<sub>7</sub>V<sub>4</sub>(P<sub>2</sub>O<sub>7</sub>)<sub>4</sub>PO<sub>4</sub> (3.88 V),<sup>16,17</sup> and Na<sub>2</sub>VOP<sub>2</sub>O<sub>7</sub> (3.8 V).<sup>18</sup> The strong inductive effect of the PO<sub>4</sub><sup>3–</sup> polyanion alters the covalent character of V–O (or –F) bonds and moderates the energetics of the vanadium redox couple, resulting in favorable operating potentials for these compounds.<sup>19–21</sup> However, most of the above electrode materials face limitations in terms of theoretical capacity (ca. 90–120 mAh g<sup>–1</sup>), because of the heavy polyanion group.<sup>12,13,16–18</sup>

The vanadium-based phosphate, NaVOPO<sub>4</sub>, characterized by a moderately high operating potential (3.6 V vs. Na<sup>+</sup>/Na) as well as a relatively large theoretical capacity (145 mAh g<sup>–1</sup>),<sup>22</sup> provides one of the highest theoretical energy densities (ca. 530 Wh kg<sup>–1</sup>) among the positive electrode materials for Na secondary batteries.<sup>10,11,15</sup> Despite such an attractive energy density, however, NaVOPO<sub>4</sub> has not been significantly explored as positive electrode material as yet. Earlier studies on NaVOPO<sub>4</sub> mostly focused on its synthesis and structural properties.<sup>23–25</sup> The only electrochemical report to date, by Song et al., revealed that 62% (90 mAh g<sup>–1</sup>) of the theoretical capacity can

76 be realized at room temperature in 1 M NaClO<sub>4</sub>/propylene carbonate (PC); however,  
77 other important electrode characteristics such as rate capability and long-term  
78 cyclability, as well as reaction mechanism, remain to be investigated.<sup>22</sup>

79 The energy density has long been considered as the most critical figure of merit  
80 for a battery, which is dominated by the performance of positive electrode materials in  
81 many Li and Na secondary batteries. On the other hand, the electrolyte also represents  
82 a key component that governs many important properties of batteries.<sup>26–28</sup> The  
83 electrolytes investigated for Na secondary batteries are mainly based on organic  
84 solvents, following similar approaches to those developed for lithium ion batteries.<sup>3,28</sup>  
85 As the interest in Na secondary batteries distributed over a much more diversified and  
86 global manner, the electrolytes of choice is not a single one.<sup>28</sup> Ionic liquids (ILs),  
87 characterized by a suite of unique properties such as nonflammability, nonvolatility,  
88 as well as good thermal and electrochemical stability, show considerable potential as  
89 advanced electrolytes.<sup>29–35</sup> Improved electrochemical performance has been  
90 demonstrated for cells adopting IL electrolytes, compared to those involving organic  
91 electrolytes.<sup>33–35</sup>

92 In our previous studies, the feasibility of a series of bis(fluorosulfonyl)amide  
93 (FSA)-based IL electrolytes for Na batteries has been verified.<sup>36–38</sup> The wide liquidus  
94 range of the Na[FSA]–[C<sub>3</sub>C<sub>1</sub>pyrr][FSA] IL (C<sub>3</sub>C<sub>1</sub>pyrr =

*N*-methyl-*N*-propylpyrrolidinium) allowed us to investigate the charge–discharge behavior of targeted electrode materials from low (253 K) to elevated temperatures (363 K).<sup>39–41</sup> The results revealed a considerable enhancement in reversible capacity and rate capability with increasing temperature for Na<sub>2</sub>MnSiO<sub>4</sub>,<sup>39</sup> Na<sub>2</sub>FeP<sub>2</sub>O<sub>7</sub>,<sup>40</sup> and Na<sub>1.56</sub>Fe<sub>1.22</sub>P<sub>2</sub>O<sub>7</sub>.<sup>41</sup> The performance of batteries with conventional organic electrolyte solvents have been rarely investigated at temperatures greater than 328 K, above which poor storage and inferior cycling behaviors are generally observed.<sup>42,43</sup> Since a concrete improvement in electrochemical properties was observed in IL electrolytes at elevated temperatures, operation at above room temperature is preferable and also practicable for electric vehicle and stationary storage applications.<sup>34</sup> In the present work, the electrochemical properties of NaVOPO<sub>4</sub> are investigated in Na[FSA]–[C<sub>3</sub>C<sub>1</sub>pyrr][FSA] IL electrolyte at 298 and 363 K. With the aim to understand the characteristics of NaVOPO<sub>4</sub> in higher detail, here we investigate the rate capability, the cyclability, as well as the structural variation of the materials upon electrochemical cycling. Furthermore, the galvanostatic intermittent titration technique (GITT) has been used to elucidate the Na intercalation kinetics within the material.

## 2. Experimental

Sodium vanadyl phosphate,  $\text{NaVOPO}_4$ , was synthesized by the sol-gel method from  $\text{Na}(\text{CH}_3\text{COO})$ ,  $\text{NH}_4\text{VO}_3$ ,  $(\text{NH}_4)_2\text{HPO}_4$  and citric acid, according to a reported procedure.<sup>22</sup> Equal amounts of the starting materials were dissolved in ultrapure water with magnetic stirring at 343 K. After a clear blue solution formed, the mixture was further dried at 353 K to transform the solution from sol to gel. The gel was initially heated at 573 K for 4 h and then at 773 K for 4 h in air. The as-prepared  $\text{NaVOPO}_4$  (denoted as NVP-AP) was thoroughly mixed with acetylene black (AB, 5:1 in weight) via a high-energy planetary ball-milling (Fritsch Pulverisette 7 Premium Line) for 2 h and 8 h at 700 rpm (the corresponding material samples are hereafter denoted as NVP/AB-2h and NVP/AB-8h, respectively).

The crystal structure of NVP-AP was determined by an X-ray diffractometer (Rigaku SmartLab) equipped with a one-dimensional high-speed Si strip detector (Rigaku D/teX Ultra), utilizing  $\text{Cu K}\alpha$  radiation (40 kV and 30 mA). The structural refinement was carried out by the Rietveld method in an iterative procedure using the RIETAN-FP program.<sup>44</sup> The crystal structure was visualized by the VESTA software.<sup>45</sup> The morphology of the sample was observed using field-emission scanning electron microscopy (FE-SEM, Hitachi SU-8020). The electrochemical properties of NVP-AP, NVP/AB-2h, and NVP/AB-8h were assessed using 2032-type coin cells with a Bio-Logic VSP potentiostat, as described in our previous reports.<sup>37,40</sup>

The positive electrode was prepared by mixing active material, vapor-grown carbon fibers (VGCFs), and polytetrafluoroethylene (PTFE) with agate mortar and pestle. The resultant NaVOPO<sub>4</sub>/conductive carbon (AB+VGCF)/PTFE weight ratio was 75:20:5. A metallic Na disc pressed onto an aluminum current collector was used as the negative electrode. The Na[FSA]–[C<sub>3</sub>C<sub>1</sub>pyrr][FSA] (20:80 molar ratio) IL was used as electrolyte according to our previous report.<sup>37,40</sup> The mass loading and thickness of the active material were approximately 2.0 mg cm<sup>-2</sup> and 50 μm. For the GITT, a current of C/20 (7.25 mA g<sup>-1</sup>) was applied for 30 min, followed by a 12 h relaxation, unless the system satisfied the 10 mV h<sup>-1</sup> stability criterion earlier.

### 3. Results and Discussion

Fig. 1 shows the X-ray diffraction (XRD) pattern and Rietveld refinement results for NVP-AP. The structure was refined in the monoclinic lattice with *P*2<sub>1</sub>/*c* space group and lattice parameters *a* = 6.51960(9) Å, *b* = 8.44576(11) Å, *c* = 7.11499(10) Å, *β* = 115.2591(4)°, *V* = 354.314(9) Å<sup>3</sup>, and *Z* = 4, which agrees well with previously reported data for microcrystalline and single crystal samples.<sup>22,23</sup> The related structural parameters are given in the Supporting Information (Table S1). No impurity was detected, as attested by the good agreement between the experimental and calculated patterns. As shown in Fig. 2a, NaVOPO<sub>4</sub> exhibits a structure built from infinite chains of VO<sub>6</sub> octahedra interconnected by PO<sub>4</sub> tetrahedra, all in a



corner-sharing fashion. The  $\text{VO}_6$  octahedra are distorted, as the vanadium atom is displaced from the square plane comprising the four equatorial oxygen atoms toward one apical oxygen atom. The  $\text{V}-\text{O}_b$  ( $\text{O}_b$  = bridging oxygen) bond lengths alternate between longer and shorter bonds, resulting in the *trans* configuration of the  $[\text{VO}_5]_\infty$  chains (Fig. 2b, c).<sup>23,25</sup> It was suggested that the distortion of the structural units and the tilted connection between them creates additional space for Na migration.<sup>46</sup>

The XRD patterns of NVP-AP, NVP/AB-2h, and NVP/AB-8h are compared in Fig. 3a. The XRD peaks of the ball-milled samples are remarkably broadened, and the degree of broadening increases with the ball-milling time, indicative of the reduction in the crystallite size. The Scherrer formula  $D = 1.33 \lambda / \beta \cos \theta$ , where  $\lambda$  is the X-ray wavelength,  $\beta$  the integral breadth of the diffraction line, and  $\theta$  the Bragg angle, was used to estimate the crystallite size from the XRD data.<sup>47</sup> The crystallite size  $D$ , calculated as the average of the values corresponding to 4 discrete diffraction peaks (110 at  $18.4^\circ$ , 111 at  $26.7^\circ$ ,  $\bar{1}12$  at  $27.4^\circ$ , and 200 at  $30.3^\circ$ ), was 106(6), 40(4), and 32(4) nm for the NVP, NVP/AB-2h, and NVP/AB-8h samples, respectively. FE-SEM images of these samples are illustrated in Fig. 3b–d. The NVP-AP sample (Fig. 3b) is composed of many submicron grains aggregated up to several microns, suggesting a considerable grain growth even at the relatively low sintering temperature of 773 K and with a short annealing time. A similar phenomenon was observed for  $\text{NaVOP}_2\text{O}_7$

synthesized at 673 K.<sup>18</sup> After ball-milling with AB (Fig. 3c and d), there was a significant reduction in particle size, to approximately 100 nm. The trend observed by FE-SEM is consistent with that highlighted by XRD.

Fig. 4a–d show the typical galvanostatic charge–discharge curves of the NVP/AB-2h and NVP/AB-8h electrodes in the three initial cycles at 5 mA g<sup>-1</sup>. For NVP/AB-2h, the galvanostatic profiles exhibit sloping curves without plateau, and the reversible capacities are 40 and 74 mAh g<sup>-1</sup> at 298 K and 363 K, respectively. In comparison with NVP/AB-2h, NVP/AB-8h shows a higher reversible capacity under the same conditions, delivering 60 and 101 mAh g<sup>-1</sup> at 298 K and 363 K, respectively, which correspond to 41% and 70% of the theoretical capacity. The average operating potential of 3.6 V *vs.* Na<sup>+</sup>/Na is noticeable, considering that this material does not contain fluorine to facilitate the inductive effect.<sup>19,21</sup> However, the capacity on the first charge is always larger than that on the first discharge, especially at 363 K, suggesting the occurrence of an anodic parasitic reaction. To account for the abnormally high initial charge capacity, charge–discharge tests were performed on electrodes consisting of only ball-milled AB. Referring to Fig. S1, a large charge capacity was observed in the first cycle, with an apparent decrease in the subsequent cycle. This indicates that a parasitic reaction involving AB occurs, after energetic ball-milling in the composite electrode, which contributes to the observed irreversible

capacity during the first cycle. However, AB does not participate in the Na storage on the subsequent cycling. In addition, the first-cycle capacity loss could also be ascribed to Na-consuming reactions, such as the formation of a passivation layer on the electrode.<sup>48</sup> For comparison, almost no Na can be extracted from NVP-AP, which is consistent with the previous report (Fig. S2).<sup>22</sup> Pure NaVOPO<sub>4</sub> may suffer from low electronic conductivity as in the case of other phosphate battery electrode materials.<sup>49</sup> The enhanced electrochemical properties of NaVOPO<sub>4</sub>/AB electrodes are therefore attributed to the fine particles in close contact with the conductive carbon matrix, and to the shortened Na transport path lengths due to the reduction in particle size.

Song et al. reported that the NaVOPO<sub>4</sub>/AB electrode exhibits a capacity of 90 mAh g<sup>-1</sup> in the voltage range of 2.0–4.4 V in NaClO<sub>4</sub>/PC electrolyte at room temperature.<sup>22</sup> Taking into account that the capacity for a positive electrode in the region above 2.5 V, 60 mAh g<sup>-1</sup> obtained in the present IL electrolyte is thus similar to that obtained in NaClO<sub>4</sub>/PC electrolyte at room temperature,<sup>22</sup> and the capacity of 101 mAh g<sup>-1</sup> measured at 363 K is quite remarkable. The voltage profiles also exhibit a substantial difference with respect to the NaClO<sub>4</sub>/PC electrolyte, namely, a more evident discharge pseudo-plateau is obtained in this study. Most importantly, the increased capacity is mainly above 3.5 V, which is essential for achieving high energy density. These results confirm that a moderately elevated operating temperature can

effectively enhance the utilization ratio of the active materials, leading to a higher capacity. Similar findings were reported by other groups<sup>33,34,50</sup> and by us.<sup>39,41</sup>

The structural evolution of NaVOPO<sub>4</sub> upon electrochemical cycling at 363 K was investigated through an *ex situ* XRD analysis. Comparison of XRD patterns for the NaVOPO<sub>4</sub>/AB electrode at different charging and discharging states are presented in Fig. S3. It can be noticed that charging of the electrode up to 4.2 V induces only slight changes in the diffraction patterns (e.g., the intensity of the 111 peak relative to that of the  $\bar{1}12$  peak increases upon charging). Since no pronounced new diffraction peaks are detected, NaVOPO<sub>4</sub> is considered to undergo topotactic Na extraction. Some structural disorder may also occur for a low Na content as broadening of the low-angle peaks is observed.<sup>51</sup> Although the quality of the XRD pattern of the electrochemically desodiated NaVOPO<sub>4</sub> was unsatisfactory, Rietveld analysis was performed under highly constrained conditions in order to determine the lattice parameters (Table S2). The result suggests that desodiation of NaVOPO<sub>4</sub> (Na<sub>0.4</sub>VOPO<sub>4</sub>) leads to a minor (~1.2%) decrease in volume, which is close to the value between  $\beta$ -LiVOPO<sub>4</sub> and  $\beta$ -VOPO<sub>4</sub>.<sup>52</sup>

The rate capability of the NVP/AB-2h and NVP/AB-8h electrodes at 363 K is shown in Fig. 5a and b. The cells were charged to 4.2 V at a constant current density of C/10 (14.5 mA g<sup>-1</sup>), and subsequently discharged to 2.5 V at various rates.

Although the discharge capacity declines with an increase in current density, a sufficiently high rate capability is realized at 363 K. Approximately 76% and 60% of the maximum capacity observed at 5 mA g<sup>-1</sup> is maintained at 5 C and 10 C, respectively, for both the NVP/AB-2h and NVP/AB-8h. The discharge capacity is still clearly discernible up to a rate of 40 C (5800 mA g<sup>-1</sup>). The long-term cycling performance of the NVP/AB-2h and NVP/AB-8h electrodes at a current density of 1 C is shown in Fig. 6a and b. Fairly stable cycling behavior with limited capacity decay is observed at 298 K for both electrodes; when cycled at 363 K, more than 74% of the initial capacity is retained after 300 cycles. The average coulombic efficiencies over the course of the entire test are higher than 99.7% for all the cells investigated. The good cyclability can be attributed to the minimal volume change experienced by NaVOPO<sub>4</sub> during Na extraction/insertion, as well as to the use of a chemically stable IL electrolyte.

The kinetic behavior of the NVP/AB-8h electrode at 298 K and 363 K was examined using the galvanostatic intermittent titration technique (GITT) (Fig. 7). As shown in Fig. 7a, a relatively small overpotential is observed in the charge curves at 298 K, while a larger overpotential is observed toward the end of discharge. This is attributed to kinetic limitations, due to the high resistance in the particles, that hinder Na<sup>+</sup> access to their centers.<sup>53</sup> Other causes, such as the concentration polarization,

may also account for the increased overpotential at the end of these curves.<sup>54</sup> The GITT curves at 363 K clearly show that the overpotential is suppressed in the full range of voltage as compared to that at 298 K, reflecting a lower kinetic barrier for Na<sup>+</sup> insertion into this material. For both temperatures, there is no evidence of a voltage plateau in the GITT data, implying that the electrochemical reaction undergoes a single-phase rather than a two-phase mechanism.<sup>55</sup> This assignment is consistent with the *ex situ* XRD results above. Assuming that Na transport in the electrode obeys Fick's second law, the chemical diffusion coefficient can be estimated from the GITT curves using the following equation:<sup>56,57</sup>

$$D_{\text{GITT}} = \frac{4}{\pi\tau} \left( \frac{m_{\text{B}} V_{\text{m}}}{M_{\text{B}} S} \right)^2 \left( \frac{\Delta E_{\text{s}}}{\Delta E_{\tau}} \right)^2 \quad (t \ll L^2/D_{\text{GITT}})$$

where  $\tau$  is the time period of the current pulse,  $m_{\text{B}}$  is the mass of the electroactive material,  $V_{\text{m}}$  and  $M_{\text{B}}$  are its molar volume and molecular weight,  $S$  is the contact area between the electrolyte and the electrode,  $\Delta E_{\text{s}}$  is the difference in the open circuit voltage measured at the end of the relaxation period for two successive steps,  $\Delta E_{\tau}$  is the difference in cell voltage during the single titration current pulse, and  $L$  is the thickness of the electrode. This equation can be applied if there is a linear correlation between  $E_{\tau}$  and  $\tau^{1/2}$  (Fig. S4). Because the contact area used is the geometric area, the term apparent chemical diffusion coefficient is used here for  $D_{\text{GITT}}$ . It must be mentioned that the actual surface area of the active material in contact with the

electrolyte in composite electrode systems depends on the particle size of the active material and its morphology, and must be larger than the geometric area, due to the penetration of electrolyte.<sup>58</sup> Care has been taken in the present study to minimize the uncertainty in electrode physical parameters by performing the GITT measurement on the same cell at 298 and 363 K. It has been suggested that this technique gives accurate results especially for small stoichiometric changes.<sup>56</sup>

Taking these aspects into consideration, the calculated  $D_{\text{GITT}}$  at the initial stages of charge and discharge is plotted as a function of cell voltage in Fig. 7b. The  $D_{\text{GITT}}$  values range from  $2 \times 10^{-12}$  to  $1 \times 10^{-11} \text{ cm}^2 \text{ s}^{-1}$  at 298 K, and from  $1 \times 10^{-11}$  to  $3 \times 10^{-11} \text{ cm}^2 \text{ s}^{-1}$  at 363 K. The diffusivity of  $\text{Na}^+$  in  $\text{NaVOPO}_4$  is enhanced by 3–5 times by increasing the temperature from 298 to 363 K, confirming the favorable kinetics at elevated temperatures, and thus leading to improved electrochemical performance. Furthermore, the obtained  $D_{\text{GITT}}$  is comparable to that observed for layered oxides,  $\text{O3-Na}[\text{Ni}_{0.25}\text{Fe}_{0.5}\text{Mn}_{0.25}]\text{O}_2$  and  $\text{Na}_2\text{Ti}_3\text{O}_7$  (*ca.*  $10^{-12}$ – $10^{-11} \text{ cm}^2 \text{ s}^{-1}$ ),<sup>59,60</sup> and is considerably higher than that of other positive electrode materials such as  $\text{Na}_4\text{Mn}_9\text{O}_{18}$  (*ca.*  $10^{-16}$ – $10^{-15} \text{ cm}^2 \text{ s}^{-1}$ )<sup>61</sup> and olivine  $\text{NaFePO}_4$  (*ca.*  $10^{-17} \text{ cm}^2 \text{ s}^{-1}$ ),<sup>62</sup> which were acquired by similar electrochemical methods. These results highlight the potential of  $\text{NaVOPO}_4$  for high-power applications, although further improvements and optimizations in synthesis and electrode formulation are required.

## 284    **4. Conclusions**

285        In order to explore the enhanced kinetics at elevated temperatures, the  
286    charge–discharge    behavior    of    NaVOPO<sub>4</sub>    was    investigated    in  
287    Na[FSA]–[C<sub>3</sub>C<sub>1</sub>pyrr][FSA] ionic liquid electrolyte at 298 and 363 K. Reversible  
288    capacities of 60 and 101 mAh g<sup>-1</sup> were achieved at 298 and 363 K, respectively, as  
289    well as adequate rate capability and cyclability. The apparent Na chemical diffusion  
290    coefficient was evaluated by GITT analysis, which indicated that the Na<sup>+</sup> diffusivity  
291    increases by 3–5 times when the temperature increased from 298 to 363 K. The  
292    combined advantages of a moderately high operating voltage (3.6 V) and a large  
293    theoretical capacity (145 mAh g<sup>-1</sup>) designate NaVOPO<sub>4</sub> as a promising positive  
294    electrode material for Na secondary batteries. Cationic substitution of NaM<sub>x</sub>V<sub>1-x</sub>OPO<sub>4</sub>  
295    (M = Ti<sup>3+</sup>, Al<sup>3+</sup>, Fe<sup>3+</sup>) may represent a promising way to boot its performance and  
296    decrease the consumption of vanadium.

## 297    **Acknowledgements**

298    This study was partly supported by Advanced Low Carbon Technology Research and  
299    Development Program (ALCA) of Japan Science and Technology Agency (JST) and  
300    Japanese Ministry of Education, Culture, Sports, Science and Technology (MEXT)  
301    program “Elements Strategy Initiative to Form Core Research Center”.

302



303     **References**

- 304     1. D. Larcher and J. M. Tarascon, *Nature Chem.*, **7**, 19 (2014).
- 305     2. V. Palomares, M. Casas-Cabanas, E. Castillo-Martinez, M. H. Han, and T. Rojo,  
306         *Energy Environ. Sci.*, **6**, 2312 (2013).
- 307     3. N. Yabuuchi, K. Kubota, M. Dahbi, and S. Komaba, *Chem. Rev.*, **114**, 11636  
308         (2014).
- 309     4. M. S. Whittingham, *Prog. Solid State Chem.*, **12**, 41 (1978).
- 310     5. S. P. Ong, V. L. Chevrier, G. Hautier, A. Jain, C. Moore, S. Kim, X. H. Ma, and G.  
311         Ceder, *Energy Environ. Sci.*, **4**, 3680 (2011).
- 312     6. M. Okoshi, Y. Yamada, A. Yamada, and H. Nakai, *J. Electrochem. Soc.*, **160**,  
313         A2160 (2013).
- 314     7. E. Jonsson and P. Johansson, *Phys. Chem. Chem. Phys.*, **14**, 10774 (2012).
- 315     8. F. Sagane, T. Abe, Y. Iriyama, and Z. Ogumi, *J. Power Sources*, **146**, 749 (2005).
- 316     9. T. Abe, H. Fukuda, Y. Iriyama, and Z. Ogumi, *J. Electrochem. Soc.*, **151**, A1120  
317         (2004).
- 318     10. P. Serras, V. Palomares, A. Goni, I. G. de Muro, P. Kubiak, L. Lezama, and T.  
319         Rojo, *J. Mater. Chem.*, **22**, 22301 (2012).
- 320     11. Y. U. Park, D. H. Seo, H. Kim, J. Kim, S. Lee, B. Kim, and K. Kang, *Adv. Funct.*  
321         *Mater.*, **24**, 4603 (2014).
- 322     12. Z. L. Jian, W. Z. Han, X. Lu, H. X. Yang, Y. S. Hu, J. Zhou, Z. B. Zhou, J. Q. Li,  
323         W. Chen, D. F. Chen, and L. Q. Chen, *Adv. Energy Mater.*, **3**, 156 (2013).
- 324     13. K. Saravanan, C. W. Mason, A. Rudola, K. H. Wong, and P. Balaya, *Adv. Energy*  
325         *Mater.*, **3**, 444 (2013).
- 326     14. J. Barker, M. Y. Saidi, and J. L. Swoyer, *Electrochem. Solid-State Lett.*, **6**, A1  
327         (2003).

- 328 15. Y. U. Park, D. H. Seo, H. S. Kwon, B. Kim, J. Kim, H. Kim, I. Kim, H. I. Yoo,  
329 and K. Kang, *J. Am. Chem. Soc.*, **135**, 13870 (2013).
- 330 16. S. Y. Lim, H. Kim, J. Chung, J. H. Lee, B. G. Kim, J. J. Choi, K. Y. Chung, W.  
331 Cho, S. J. Kim, W. A. Goddard, Y. Jung, and J. W. Choi, *Proc. Nat. Acad. Sci.*  
332 *U.S.A.*, **111**, 599 (2014).
- 333 17. C. Deng and S. Zhang, *ACS Appl. Mater. Interfaces*, **6**, 9111 (2014).
- 334 18. P. Barpanda, G. D. Liu, M. Avdeev, and A. Yamada, *ChemElectroChem*, **1**, 1488  
335 (2014).
- 336 19. A. K. Padhi, K. S. Nanjundaswamy, C. Masquelier, S. Okada, and J. B.  
337 Goodenough, *J. Electrochem. Soc.*, **144**, 1609 (1997).
- 338 20. A. Gutierrez, N. A. Benedek, and A. Manthiram, *Chem. Mater.*, **25**, 4010  
339 (2013).
- 340 21. B. C. Melot, D. O. Scanlon, M. Reynaud, G. Rousse, J. N. Chotard, M. Henry,  
341 and J. M. Tarascon, *ACS Appl. Mater. Interfaces*, **6**, 10832 (2014).
- 342 22. J. Song, M. W. Xu, L. Wang, and J. B. Goodenough, *Chem. Commun.*, **49**, 5280  
343 (2013).
- 344 23. K. H. Lii, C. H. Li, T. M. Chen, and S. L. Wang, *Z. Kristallogr.*, **197**, 67 (1991).
- 345 24. E. J. Baran, M. B. Vassallo, and K. H. Lii, *J. Raman Spectrosc.*, **25**, 199 (1994).
- 346 25. S. Boudin, A. Guesdon, A. Leclaire, and M. M. Borel, *Int. J. Inorg. Mater.*, **2**, 561  
347 (2000).
- 348 26. B. C. Melot and J. M. Tarascon, *Acc. Chem. Res.*, **46**, 1226 (2013).
- 349 27. A. Ponrouch, R. Dedryvere, D. Monti, A. E. Demet, J. M. A. Mba, L. Croguennec,  
350 C. Masquelier, P. Johansson, and M. R. Palacin, *Energy Environ. Sci.*, **6**, 2361  
351 (2013).
- 352 28. A. Ponrouch, D. Monti, A. Boschini, B. Steen, P. Johansson, and M. R. Palacin, *J.*  
353 *Mater. Chem. A*, **3**, 22 (2015).

- 354 29. M. Armand, F. Endres, D. R. MacFarlane, H. Ohno, and B. Scrosati, *Nature*  
355 *Mater.*, **8**, 621 (2009).
- 356 30 D. R. MacFarlane, N. Tachikawa, M. Forsyth, J. M. Pringle, P. C. Howlett, G. D.  
357 Elliott, J. H. Davis, M. Watanabe, P. Simon, and C. A. Angell, *Energy Environ.*  
358 *Sci.*, **7**, 232 (2014).
- 359 31. D. Monti, E. Jonsson, M. R. Palacin, and P. Johansson, *J. Power Sources*, **245**,  
360 630 (2014).
- 361 32. H. Yoon, H. J. Zhu, A. Hervault, M. Armand, D. R. MacFarlane, and M. Forsyth,  
362 *Phys. Chem. Chem. Phys.*, **16**, 12350 (2014).
- 363 33. L. S. Plashnitsa, E. Kobayashi, Y. Noguchi, S. Okasa, and J. Yamaki, *J.*  
364 *Electrochem. Soc.*, **157**, A536 (2010).
- 365 34. N. Wongittharom, C. H. Wang, Y. C. Wang, C. H. Yang, and J. K. Chang, *ACS*  
366 *Appl. Mater. Interfaces*, **6**, 17564 (2014).
- 367 35. L. G. Chagas, D. Buchholz, L. M. Wu, B. Vortmann, and S. Passerini, *J. Power*  
368 *Sources*, **247**, 377 (2014).
- 369 36. A. Fukunaga, T. Nohira, Y. Kozawa, R. Hagiwara, S. Sakai, K. Nitta, and S.  
370 Inazawa, *J. Power Sources*, **209**, 52 (2012).
- 371 37. C. S. Ding, T. Nohira, K. Kuroda, R. Hagiwara, A. Fukunaga, S. Sakai, K. Nitta,  
372 and S. Inazawa, *J. Power Sources*, **238**, 296 (2013).
- 373 38. K. Matsumoto, T. Hosokawa, T. Nohira, R. Hagiwara, A. Fukunaga, K. Numata,  
374 E. Itani, S. Sakai, K. Nitta, and S. Inazawa, *J. Power Sources*, **265**, 36 (2014).
- 375 39. C. Y. Chen, K. Matsumoto, T. Nohira, and R. Hagiwara, *Electrochem. Commun.*,  
376 **45**, 63 (2014).
- 377 40. C. Y. Chen, K. Matsumoto, T. Nohira, C. S. Ding, T. Yamamoto, and R.  
378 Hagiwara, *Electrochim. Acta*, **133**, 583 (2014).

- 379 41. C. Y. Chen, K. Matsumoto, T. Nohira, and R. Hagiwara, *J. Electrochem. Soc.*, **162**,  
380 A176 (2015).
- 381 42. K. Amine, J. Liu, and I. Belharouak, *Electrochem. Commun.*, **7**, 669 (2005).
- 382 43. F. Mestre-Aizpurua, S. Hamelet, C. Masquelier, and M. R. Palacin, *J. Power*  
383 *Sources*, **195**, 6897 (2010).
- 384 44. F. Izumi and K. Momma, *Solid State Phenom.*, **130**, 15 (2007).
- 385 45. K. Momma and F. Izumi, *J. Appl. Crystallogr.*, **44**, 1272 (2011).
- 386 46. R. Tripathi, S. M. Wood, M. S. Islam, and L. F. Nazar, *Energy Environ. Sci.*, **6**,  
387 2257 (2013).
- 388 47. A. L. Patterson, *Phys. Rev.*, **56**, 978 (1939).
- 389 48. S. Komaba, T. Ishikawa, N. Yabuuchi, W. Murata, A. Ito, and Y. Ohsawa, *ACS*  
390 *Appl. Mater. Interfaces*, **3**, 4165 (2011).
- 391 49. C. Delacourt, L. Laffont, R. Bouchet, C. Wurm, J. B. Leriche, M. Morcrette, J. M.  
392 Tarascon, and C. Masquelier, *C. J. Electrochem. Soc.*, **152**, A913 (2005).
- 393 50. N. Wongittharom, T. C. Lee, C. H. Wang, Y. C. Wang, and J. K. Chang, *J.*  
394 *Mater. Chem. A*, **2**, 5655 (2014).
- 395 51. K. Trad, D. Carlier, L. Croguennec, A. Wattiaux, B. Lajmi, M. Ben Amara, and C.  
396 Delmas, *J. Phys. Chem. C*, **114**, 10034 (2010).
- 397 52. J. Gaubicher, T. Le Mercier, Y. Chabre, J. Angenault, and M. Quarton, *J.*  
398 *Electrochem. Soc.*, **146**, 4375 (1999).
- 399 53. J. Liu, D. H. Chang, P. Whitfield, Y. Janssen, X. Q. Yu, Y. N. Zhou, J. M. Bai, J.  
400 Ko, K. W. Nam, L. J. Wu, Y. M. Zhu, M. Feyngenson, G. Amatucci, A. Van der  
401 Ven, X. Q. Yang, and P. Khalifah, *Chem. Mater.*, **26**, 3295 (2014).
- 402 54. Z. L. Jian, H. J. Yu, and H. S. Zhou, *Electrochem. Commun.*, **34**, 215 (2013).
- 403 55. R. Berthelot, D. Carlier, and C. Delmas, *Nature Mater.*, **10**, 74 (2011).
- 404 56. W. Weppner and R. A. Huggins, *J. Electrochem. Soc.*, **124**, 1569 (1977).

- 405 57. C. Delacourt, M. Ati, and J. M. Tarascon, *J. Electrochem. Soc.*, **158**, A741 (2011).
- 406 58. K. M. Shaju, G. V. S. Rao, and B. V. R. Chowdari, *J. Mater. Chem.*, **13**, 106
- 407 (2003).
- 408 59. S. M. Oh, S. T. Myung, C. S. Yoon, J. Lu, J. Hassoun, B. Scrosati, K. Amine, and
- 409 Y. K. Sun, *Nano Lett.*, **14**, 1620 (2014).
- 410 60. A. Rudola, K. Saravanan, C. W. Mason, and P. Balaya, *P. J. Mater. Chem. A*, **1**,
- 411 2653 (2013).
- 412 61. Y. L. Cao, L. F. Xiao, W. Wang, D. W. Choi, Z. M. Nie, J. G. Yu, L. V. Saraf, Z.
- 413 G. Yang, and J. Liu, *Adv. Mater.*, **23**, 3155 (2011).
- 414 62. Y. J. Zhu, Y. H. Xu, Y. H. Liu, C. Luo, and C. S. Wang, *Nanoscale*, **5**, 780 (2013).

## Figure captions

**Figure 1.** X-ray diffraction pattern with Rietveld refinement of NaVOPO<sub>4</sub> ( $R_{wp} = 4.38\%$  and  $R_p = 3.13\%$ ): experimental data (red dots), calculated pattern (black line), Bragg positions (green bars) and difference curve (blue line).

**Figure 2.** Structure of NaVOPO<sub>4</sub>. (a) Crystal structure of NaVOPO<sub>4</sub>, with VO<sub>6</sub> and PO<sub>4</sub> polyhedra shown in blue and gray, respectively. The Na, Fe and O atoms are colored green, navy, and orange, respectively; (b) distorted VO<sub>6</sub> octahedral unit; (c) a [VO<sub>5</sub>]<sub>∞</sub> chain in trans configuration with staggered VO<sub>6</sub> octahedra.

**Figure 3.** (a) X-ray diffraction patterns of as-prepared NaVOPO<sub>4</sub> (NVP-AP) and NaVOPO<sub>4</sub> ball milled with AB for 2 h and 8 h (NVP/AB-2h and NVP/AB-8h). SEM images of (b) NVP, (c) NVP/AB-2h, and (d) NVP/AB-8h.

**Figure 4.** Galvanostatic charge–discharge curves for the NVP/AB-2h and NVP/AB-8h electrodes: Na/Na[FSA]–[C<sub>3</sub>C<sub>1</sub>pyrr][FSA]/NVP/AB-2h cell at (a) 298 K and (b) 363 K; Na/Na[FSA]–[C<sub>3</sub>C<sub>1</sub>pyrr][FSA]/NVP/AB-8h cell at (c) 298 K and (d) 363 K. Cut-off voltage: 2.5–4.2 V. Current density: 5 mA g<sup>−1</sup>. Note the different capacity scale in panel (d).

**Figure 5.** Discharge curves of the (a) NVP/AB-2h and (b) NVP/AB-8h electrodes at various current densities at 363 K. The cells were charged to 4.2 V at a constant rate of C/10 ( $14.5 \text{ mA g}^{-1}$ ).

**Figure 6.** Cycling performance and coulombic efficiency (C.E.) of the (a) NVP/AB-2h and (b) NVP/AB-8h electrodes at 298 and 363 K. Cut-off voltage: 2.5–4.2 V. Current density: 1 C ( $145 \text{ mA g}^{-1}$ ).

**Figure 7.** (a) GITT evaluation of the NVP/AB-8h electrode at 298 K and 363 K. Conditions: 30 min charging/discharging segments at C/20 ( $7.25 \text{ mA g}^{-1}$ ) followed by 12 h relaxation. (b) Chemical diffusion coefficient of Na ions in  $\text{NaVOPO}_4$  ( $D_{\text{GITT}}$ ) calculated from GITT as a function of cell voltage during charge (open symbols) or discharge (solid symbols).

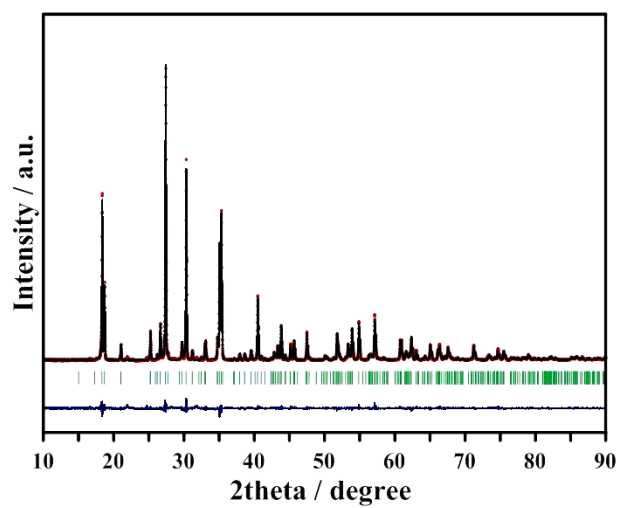


Figure 1

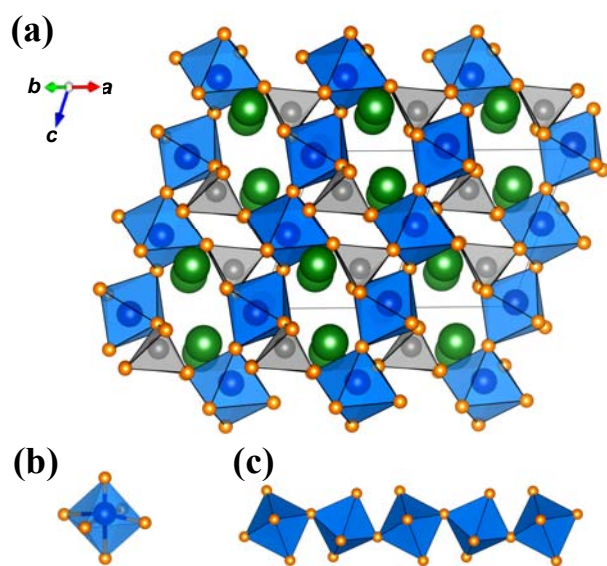


Figure 2



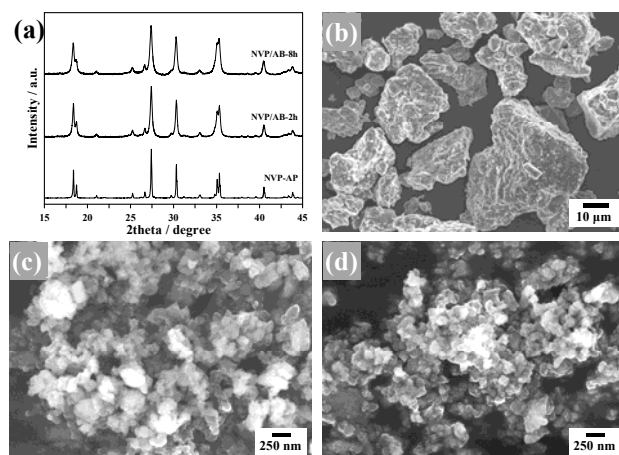


Figure 3

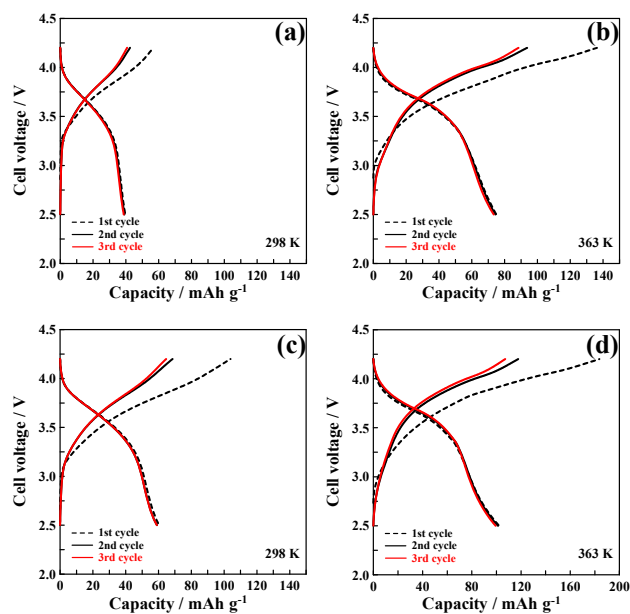


Figure 4

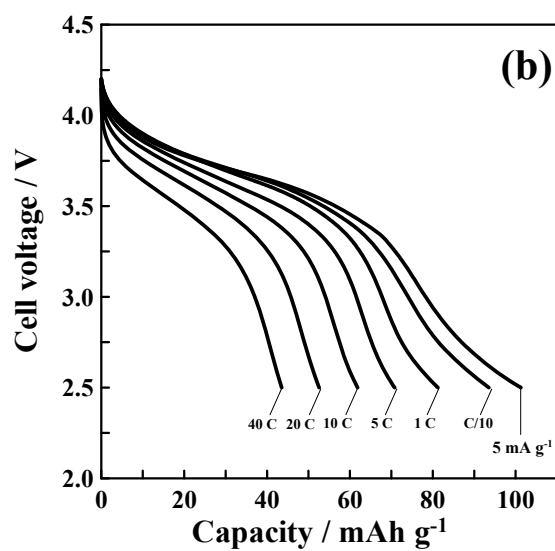
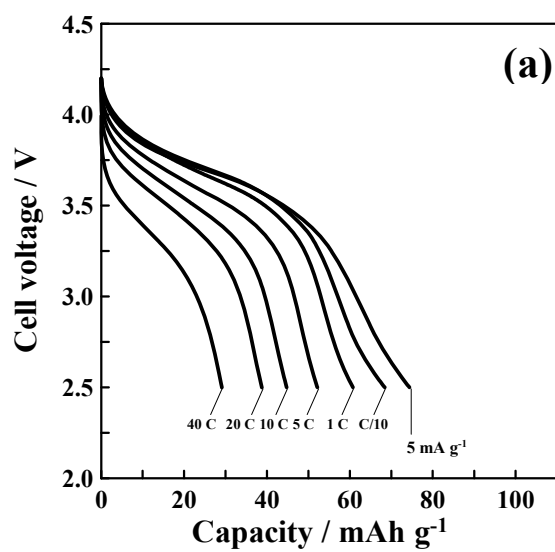


Figure 5

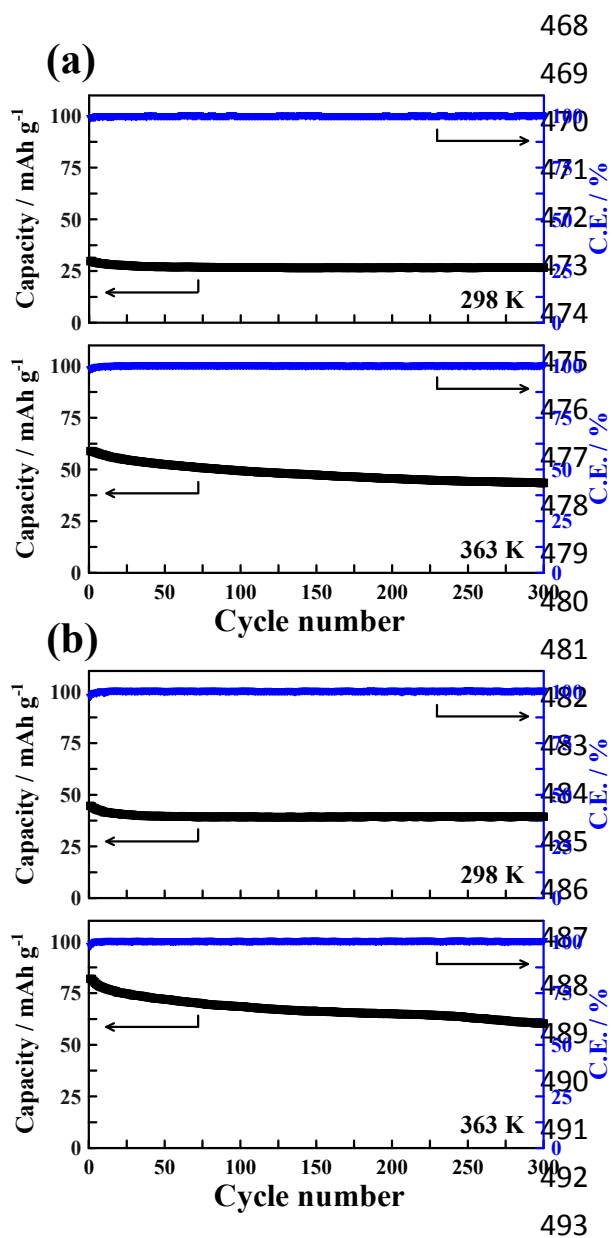


Figure 6

